Charge−Discharge Properties of Sn_4P_3 Negative Electrode in Ionic Liquid Electrolyte for Na-Ion Battery

Hiroyuki Usui[†,§], *Yasuhiro Domi*[†,§], *Kohei Fujiwara*[†,§], *Masahiro Shimizu*[†,§], *Takayuki Yamamoto*[‡], *Toshiyuki Nohira*[||], *Rika Hagiwara*[‡], *and Hiroki Sakaguchi*[*,†,§]

[†] Department of Chemistry and Biotechnology, Graduate School of Engineering, Tottori University, 4-101 Minami, Koyama-cho, Tottori 680-8552, Japan

[§] Center for Research on Green Sustainable Chemistry, Tottori University, 4-101 Minami, Koyama-cho, Tottori 680-8552, Japan

[‡] Graduate School of Energy Science, Kyoto University, Sakyo-ku, Kyoto 606-8501, Japan

[||] Institute of Advanced Energy, Kyoto University, Uji 611-0011, Japan

Corresponding Author

* Tel./Fax: +81-857-31-5265, E-mail: sakaguch@chem.tottori-u.ac.jp

ABSTRACT

We evaluated the charge-discharge performance of Sn_4P_3 negative electrode in an ionic liquid electrolyte comprised of *N*-methyl-*N*-propylpyrrolidinium bis(fluorosulfonyl)amide (Py13-FSA) and NaFSA. We also conducted cyclic voltammetry and transmission electron microscopy for the Sn_4P_3 electrode to reveal the reaction mechanism. It was suggested that $Na_{15}Sn_4$ and Na_3P are formed via its phase separation in the first sodiation, and that elemental Sn and elemental P formed by the following desodiation respectively react with Na ions in the subsequent cycles. The Sn_4P_3 electrode exhibited a high Coulombic efficiency of 99.1% at the 4th cycle and an excellent cycling performance with a high reversible capacity of 750 mA h g^{-1} even at the 200th cycle. We demonstrated that there are two important factors to improve the performance: i) higher volume fraction of Sn than P, and ii) uniform dispersion of Sn nanoparticles in P matrix. The ionic liquid electrolyte showed a good applicability to the Sn_4P_3 negative electrode due to its superior electrochemical stability.

Table of Contents Graphic

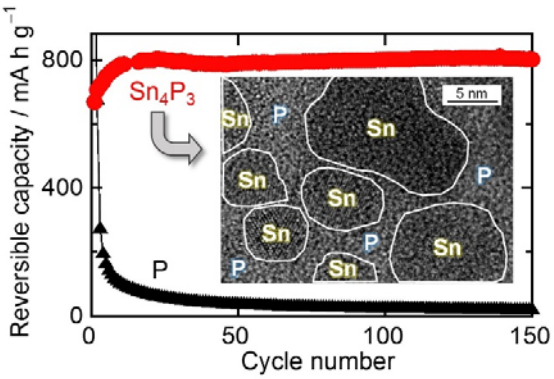

Na-ion batteries (NIBs) are attracting much interests for large-scale energy storage because of the low cost, natural abundance, wide distribution of sodium resources. The operation mechanisms of Li-ion battery (LIB) and NIB are very similar to each other because charge−discharge reactions occur by insertion/extraction of alkali metal ions into/from active materials of negative and positive electrodes. Compared with Li^+, a 2.4 times larger ionic volume of Na^+ and the resulting slower kinetics prevent host materials of negative and positive electrodes from achieving fast and stable Na^+ insertion and extraction[1]. Recently, some researchers have developed prospective positive electrode material candidates: $NaFeO_2$,[2] $Na_x[Fe_{1/2}Mn_{1/2}]O_2$,[3] and $Na_2Fe_2(SO_4)_3$[4]. On the other hand, there still remains a challenge to develop promising negative electrode materials. A hard carbon is one of the promising candidates of negative electrode materials. It has been reported that the hard carbon electrodes exhibited stable cyclabilities and reversible capacities of 220−260 mA h g^{-1} for 100 charge−discharge cycles[5-7]. A practical application of NIB, however, requires more advanced performance with regard to reversible capacity, cyclability, and rate capability.

For developing high capacity negative electrodes, researchers have focused some Na-storage elements, phosphorus (P)[8], tin (Sn)[9-11], silicon (Si)[12,13], antimony (Sb)[14,15], and germanium (Ge)[16,17]. Based on alloying/dealloying reactions with Na, these elements have high theoretical capacities (Na_3P: 2596 mA h g^{-1}, $Na_{15}Sn_4$: 847 mA h g^{-1}, $Na_{0.76}Si$[12]: 725 mA h g^{-1}, Na_3Sb: 660 mA h g^{-1}, and NaGe: 369 mA h g^{-1}). Among these elements, P and Sn are particularly attractive because of their high theoretical capacities. The disintegration of active material layers is, however, induced by their significant volume expansions (Na_3P: 490%, $Na_{15}Sn_4$: 525%) and a tin's aggregation during charge−discharge reactions. In addition, Na_3P has a very poor electronic conductivity. The disintegration and the low conductivity lead to an electrical isolation of the

active material layer and the resulting rapid capacity decays of P[18] and Sn[19] negative electrodes. For this problem, Yang *et al.*[20], Kim *et al.*[21], and the authors[22] have revealed that the Sn_4P_3 negative electrodes exhibited better cycling performances in conventional organic electrolytes than the P and Sn negative electrodes. The improvements in the performances are probably attributed to complementary effects of Sn and Na_3P formed by sodiation of P: metallic Sn acts as a conducting pathway to activate the reversible sodiation of nonconductive Na_3P phase, while the Na_3P phase provides a shield matrix preventing Sn aggregation. In addition, the authors have found for the first time that further improvement in the performance was attained by applying an ionic liquid electrolyte to the Sn_4P_3 negative electrode[22]. However, the detailed mechanism for the improvement has not been sufficiently explored yet. In this study, we investigated the mechanism of the improvement by comparing the Sn_4P_3 with a P-rich compound (SnP_3). Moreover, we studied the effect of electrolytes on the charge-discharge performance of Sn_4P_3 negative electrode by using another kind of ionic liquid and an organic electrolyte.

Active material powders of Sn_4P_3 and SnP_3 were prepared by a mechanical alloying (MA) method using tin and black phosphorous with weight ratios of 4:3 and 1:3, respectively. The mixtures of tin and phosphorous powders were put in a stainless steel vessel together with balls so that the weight ratio of the active material and the balls was 1:30. The MA was carried out by using a high-energy planetary ball mill (P-6, Fritsch) for 10 hours with a rotation speed of 380 rpm at room temperature to obtain Sn_4P_3 and SnP_3 powders. The crystal structures and the morphologies of the powders were observed by using an X-ray diffraction (XRD, Ultima IV, Rigaku) and a field emission scanning electron microscope (FE-SEM, JSM-6701F, JEOL Ltd.) as shown in Fig. S1. The nanostructure of the Sn_4P_3 powder was observed by a field-emission

transmission electron microscopy (TEM, HF-2000, Hitachi Ltd.). It was confirmed that the Sn_4P_3 powder has the particle size of 45.0±6.7 nm (Fig. S2).

Conventional slurry-based electrodes were prepared by using a mixture of the active material powders, conductive additive of acetylene black (AB), and binder of carboxymethyl cellulose (CMC) and styrene-butadiene rubber (SBR). The weight ratio of active material/AB/CMC/SBR was 70/15/10/5 wt.%. The slurry was pasted on an Al foil current collector, and was dried to form an active material layer. The loading amount and the film thickness of active material layer were 1.6 mg cm^{-2} and 15 μm, respectively. Na-insertion/extraction properties of the electrodes were evaluated in 2032-type coin cells using a counter electrode of Na metal sheet. We used an ionic liquid electrolyte comprised of 1 M sodium bis(fluorosulfonyl)amide (NaFSA)-dissolved in *N*-methyl-*N*-propylpyrrolidinium bis(fluorosulfonyl)amide (Py13-FSA or C_3C_1pyrrFSA). For comparison, we also used 1-ethyl-3-methylimidazolium bis(fluorosulfonyl)amide (EMI-FSA or C_2C_1imFSA) as another kind of ionic liquid and propylene carbonate (PC) as an organic electrolyte. Galvanostatic charge–discharge tests were carried out using an electrochemical measurement system (HJ-1001 SM8A, Hokuto Denko Co., Ltd.) at 303 K with potential ranges of 0.005−2.000 V vs. Na^+/Na. The current densities were set to be 50 mA g^{-1}, which corresponds to C-rates of 0.044C for Sn_4P_3 and 0.031C for SnP_3.

Figure 1 shows the initial charge−discharge curves for Sn, P (black phosphorus), Sn_4P_3 and SnP_3 electrode in an ionic liquid electrolyte (NaFSA/Py13-FSA). The Sn_4P_3 electrode and the SnP_3 electrode delivered the initial discharge (desodiation) capacities of 670 mA h g^{-1} and 1100 mA h g^{-1}, respectively, which are higher than that of Sn electrode (410 mA h g^{-1}). The capacity enhancement is probably contributed by the existence of P with the highest theoretical capacity (2596 mA h g^{-1} by itself) in the active materials. The Sn_4P_3 electrode and the SnP_3 electrode exhibited the initial Coulombic efficiencies of 83.5% and 88.4%, respectively, which are higher than that of the Sn electrode (72.5%). In particular, the Sn_4P_3 electrode maintained very high efficiencies after the 2nd cycle, and attained as high as 99.1% at the 4th cycle as shown in Fig. S3. Such high efficiencies have never been achieved for Sn_4P_3 electrodes in conventional organic electrolytes by other researchers[20,21,23,24]. This results indicates that the ionic liquid electrolyte

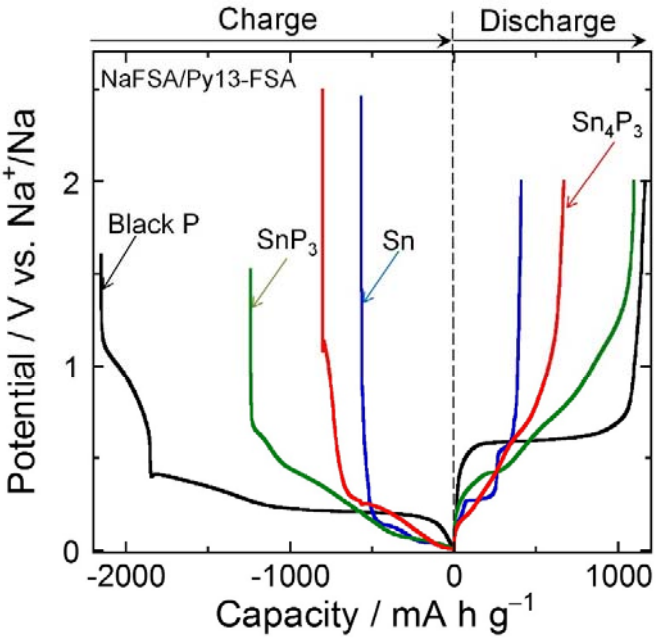

Figure 1. Charge-discharge curves at the first cycles for Sn_4P_3 electrode and SnP_3 electrode in ionic liquid electrolyte of NaFSA/Py13-FSA.

has a good applicability to the Sn_4P_3 electrode.

Figure 2 represents cycling performances of these electrodes. The Sn electrode showed a rapid capacity decay by the 10th cycle, resulting in an inferior performance to the hard carbon electrode[7]. Although a high initial capacity of 1160 mA h g^{-1} was observed for the P electrode, the capacity drastically decreased in the initial few cycles. These capacity decays are attributable to the significant volume changes of Sn and P during the charge−discharge reactions, and the resulting disintegration of the active material layers[18,19]. The capacity of the SnP_3 electrode also steeply dropped in the initial several cycles. On the other hand, the Sn_4P_3 electrode showed a gradual increase in the capacity for the initial 10 cycles, and maintained high capacities of 800 mA h g^{-1} until the 100th cycle. To elucidate the origin of such excellent performance, we carried out cyclic voltammetry and TEM observations.

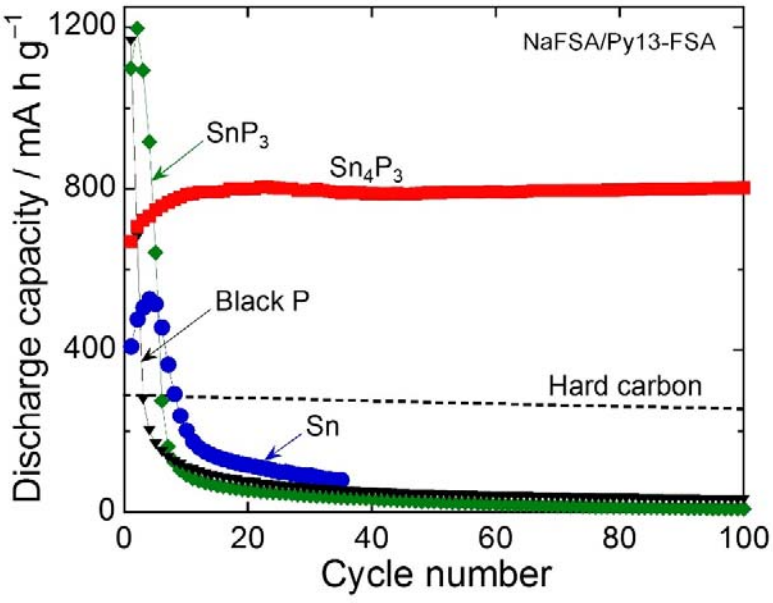

Figure 2. Cycling performances of Sn_4P_3 electrode and SnP_3 electrode in ionic liquid electrolyte of NaFSA/Py13-FSA. For comparison, the capacities of hard carbon electrode[7] were also plotted.

Figure 3 shows cyclic voltammograms of the Sn_4P_3 electrode in the initial three cycles. At the first cycle, a cathodic current peak appeared in the potential range from 0.4 to 0 V vs. Na^+/Na. This peak originates from the sodiation reaction of Sn_4P_3 to form Na_3P and $Na_{15}Sn_4$ phases[20,24]. In the anodic process, two peaks can be recognized at 0.4 and 0.7 V vs. Na^+/Na. The former results from desodiation of Na−Sn phases ($Na_{15}Sn_4$ and Na_9Sn_4)[20,25]. The latter is caused by

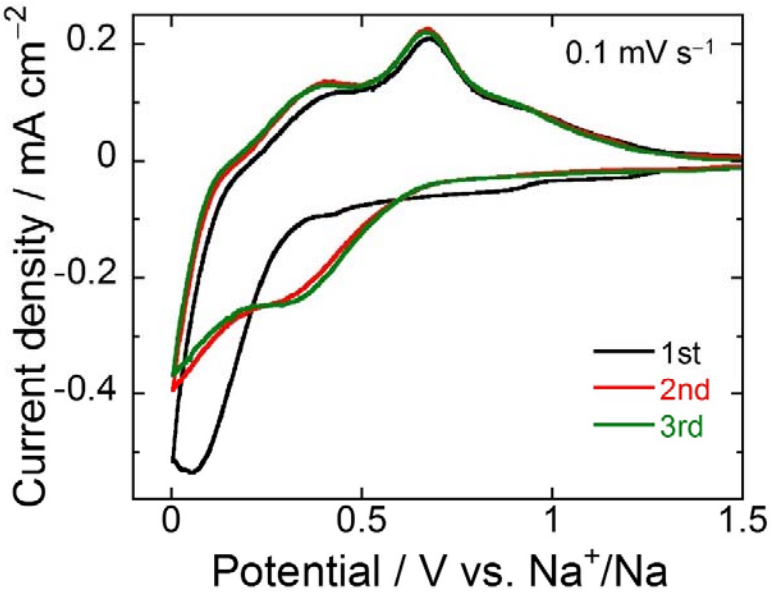

Figure 3. Cyclic voltammograms of Sn_4P_3 electrode in ionic liquid electrolyte of NaFSA/Py13-FSA. The measurement was carried out by using three electrode cell under the seep rate of 0.1 mV s^{-1}.

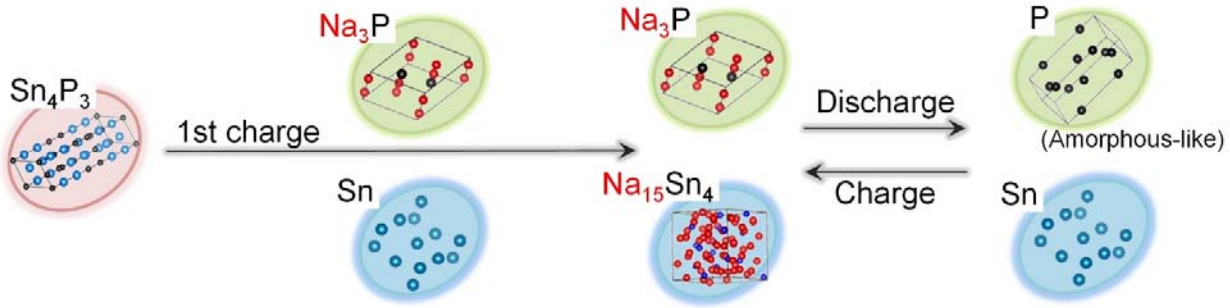

Figure 4. Phase transformation of Sn_4P_3 by sodiation and desodiation reactions.

desodiation of Na-poorer Na−Sn phases (NaSn and $NaSn_3$)[20,25] and Na_3P phase[26]. In the subsequent cycles, a cathodic peak was observed at 0.4 V vs. Na^+/Na and a cathodic current rise was observed at 0.2 V, which correspond to sodiation reactions of elemental P[26] and elemental Sn[25], respectively. Summarizing the above, the reaction mechanism is illustrated in Figure 4. The figure of the crystal structures was created using VESTA package by K. Momma and F. Izumi[27]. As several researchers have reported[20-22], we confirmed that the electrode reaction occurs as follows: Sn_4P_3 phase forms $Na_{15}Sn_4$ and Na_3P via its phase separation in the first sodiation, and elemental Sn and elemental P individually react with Na ions at different potential regions in the subsequent cycles.

Figure 5 displays results of TEM observations for Sn_4P_3 particles on a Cu grid after the first desodiation. No Scherrer ring was observed for the corresponding selected electron diffraction (Fig.S4), demonstrating that crystalline Sn_4P_3 phase changed to amorphous-like phase and/or nanocrystalline phase with several nanometers in size. Crystallites with dark contrast were observed in the TEM image, and their sizes were 5.7±1.3 nm (Fig. 5(a)). Two kinds of lattice fringes with different spacings were recognized in the crystallites (Fig.5(b)). The fringe spacings of d_1 and d_2 were estimated to be approximately 0.288 and 0.278 nm, and the two fringe directions make an angle of 62°. The d_1 and d_2 are almost equivalent with lattice spacings of d_{200}

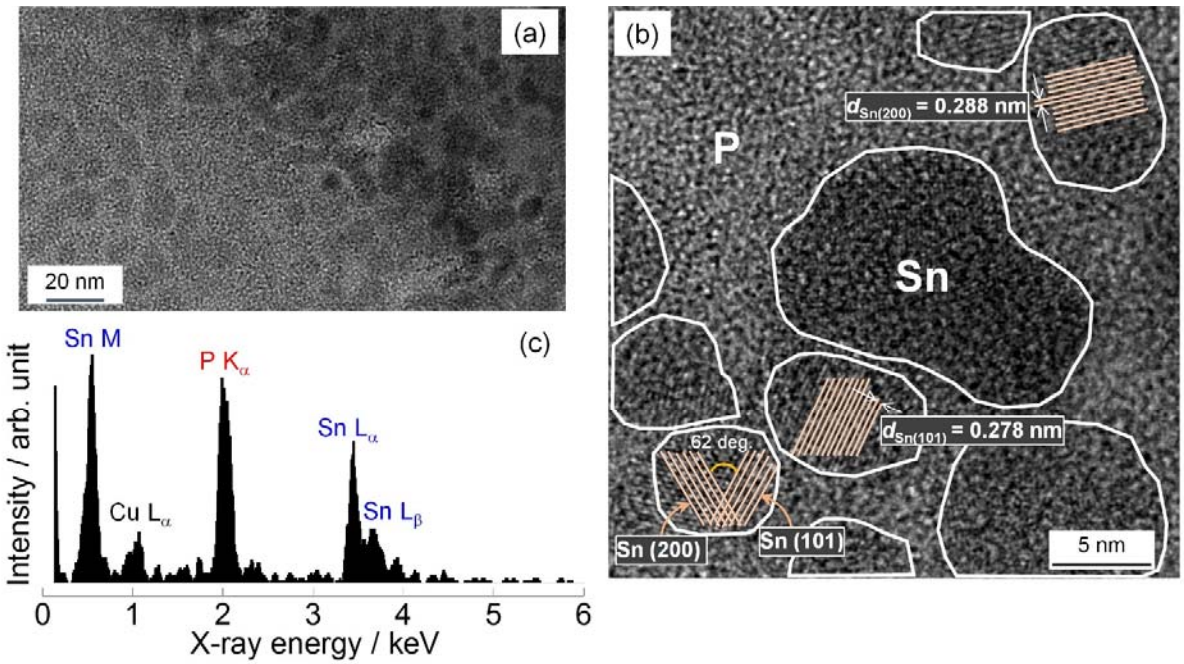

Figure 5. (a) TEM image of Sn_4P_3 after the first desodiation. The particle size was 5.7±1.3 nm. (b) High-magnification TEM image of the particles. (c) Corresponding elemental analysis result for Sn_4P_3 on Cu grid by energy dispersive X-ray spectroscopy.

(0.2915 nm) and d_{101} (0.2793 nm) in β-Sn (Inorganic Crystal Structure Database, ICSD No. 00-004-0673. The crossing angle of the (100) and (101) planes is 61.4°.). The lattice alignment of the crystallites corresponds to that of Sn observed in the direction along the [010] zone axis. We therefore concluded that the crystallites are crystallized Sn nanoparticles formed by the first desodiation. In contrast, no lattice fringe was found for P phase. An elemental analysis, however, detected not only Sn but also P (Fig.5(c)), indicating that an amorphous-like P exists in bright contrast regions. It was consequently revealed that the first desodiation of Sn_4P_3 forms nanostructured domains in which crystalline Sn nanoparticles are dispersed in the amorphous-like P matrix. Owing to the nanostructure formation, the P matrix could suppress aggregation of Sn nanoparticles, and metallic Sn complements the poor electronic conductivity of Na_3P[20,22], which contributes to the high Coulombic efficiencies and the excellent cycling performance. On the other hand, the capacity steeply dropped during the initial several cycles in case of P-richer Sn−P phase (SnP_3). We consider that metallic Sn could not effectively complement the poor

conductivity of Na_3P because of the smaller amount Sn in SnP_3. It was thus demonstrated that there are two important factors to improve the charge−discharge performance: i) the higher volume fraction of Sn than P (Fig.S5), and ii) the uniform dispersion of Sn nanoparticles in P matrix.

To evaluate the applicability of Py13-FSA as an electrolyte for the Sn_4P_3 electrode, we used another ionic liquid electrolyte (NaFSA/EMI-FSA) and an organic electrolyte (sodium bis(trifluoromethanesulfonyl)amide-dissolved in PC, NaTFSA/PC). In our previous study[12], it has been found that NaTFSA is more preferable as Na salt for organic electrolyte than NaFSA. No significant difference was found for the initial capacities and Coulombic efficiencies (Fig.S6). However, in the organic electrolyte, we observed remarkable decreases in capacity and Coulombic efficiency for the initial 20 cycles as shown in Fig. 6. When NaFSA/EMI-FSA ionic liquid was used, capacity decays were continuously observed for 80 cycles. The Coulombic

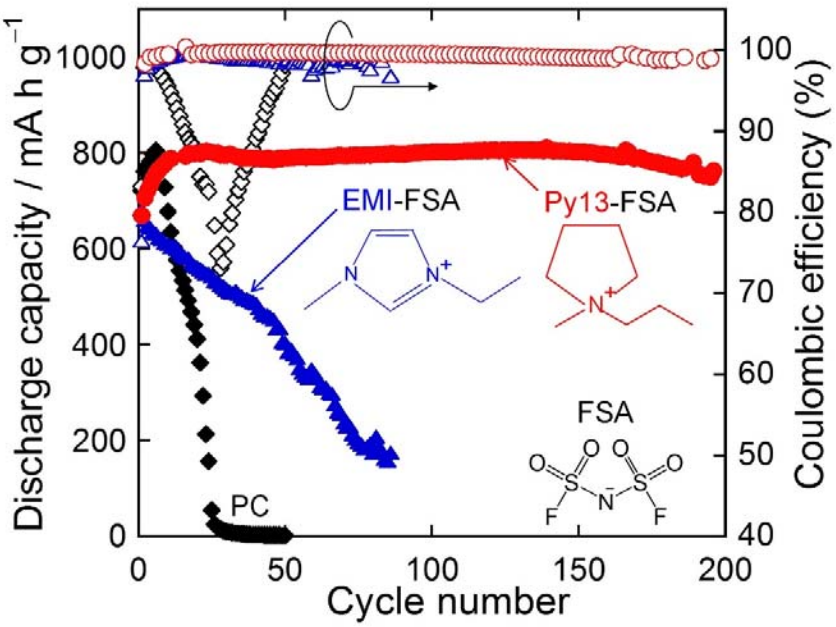

Figure 6. Cycling performances and Coulombic efficiencies of Sn_4P_3 electrode in various electrolytes using solvents of Py13-FSA, EMI-FSA, and PC.

efficiencies were inferior to those obtained in Py13-FSA for every cycle. In contrast, a high capacity of 750 mA h g^{-1} was maintained even at the 200th cycle in Py13-FSA. We suggest that the capacity decays for PC and EMI-FSA arise from their cathodic decompositions and the resulting formation of a non-uniform surface film on electrode. The decomposition of EMI cations occurs by an initial attack on an acidic proton attached to the C2 ring carbon between two nitrogen, which leads to a successive alkylation of the ring[28]. As the authors have demonstrated for the Si negative electrode for LIB[29], the non-uniform surface film causes intensive sodiation/desodiation reactions on local region of the electrode surface, resulting in the Sn particle aggregation and the disintegration of the active material layer. The electrochemical stability of PC solvent is much inferior to ionic liquids, which leads to significant decomposition of PC-based electrolytes and the resulting capacity decays for LIB anodes[29-31] and NIB anodes[19,22]. A superior electrochemical stability of Py13 cation can suppress the cathodic decomposition and the formation of non-uniform surface film, thereby providing the excellent cycling performance of the Sn_4P_3 electrode in the Py13-FSA electrolyte. This electrolyte delivered not only the excellent cyclability but also a good rate-capability: the electrode exhibited a discharge capacity of 520 mA h g^{-1} even at high current density of 1000 mA g^{-1} (0.82C) (Fig.S7). In our strategy, ionic liquid electrolyte should have an important role to effectively extract an excellent performance of Sn_4P_3 electrode. The important role is to suppress the continuous cathodic decomposition of the electrolyte because of its high electrochemical stability. These results demonstrated that Py13-FSA is very favorable electrolyte for the Sn_4P_3 electrode to bring out the performance to the maximum.

In summary, we evaluated the charge−discharge performance of the Sn_4P_3 negative electrode in NaFSA/Py13-FSA ionic liquid. The reaction mechanism was investigated by cyclic

voltammetry and TEM observation for the Sn_4P_3 electrode. We confirmed that $Na_{15}Sn_4$ and Na_3P are formed via its phase separation in the first sodiation, and that elemental Sn and elemental P individually react with Na ions in the subsequent cycles. The electrode showed the excellent performance with the capacity of 750 mA h g^{-1} at the 200th cycle. We demonstrated that there are two important factors to improve the performance: i) higher volume fraction of Sn than P, and ii) uniform dispersion of Sn nanoparticles in P matrix. The excellent performance is also attributed to the good applicability of this ionic liquid electrolyte with superior electrochemical stability.

ACKNOWLEDGMENT

This study was partially supported by Advanced Low Carbon Technology Research and Development Program (ALCA), Joint Usage/Research Program on Zero-Emission Energy Research, Institute of Advanced Energy, Kyoto University (ZE27A-10, ZE28A-21), and Japan Society for the Promotion of Science (JSPS) KAKENHI (Grant Number 17H03128, 17K17888, 16K05954). A part of this work was supported by "Advanced Characterization Nanotechnology Platform, Nanotechnology Platform Program of the Ministry of Education, Culture, Sports, Science and Technology (MEXT), Japan" at the Research Center for Ultra-High Voltage Electron Microscopy (Nanotechnology Open Facilities) in Osaka University. The authors thank Prof. H. Yasuda and Dr. T. Sakata for their helpful assistances in HR-TEM observations.

ASSOCIATED CONTENT

Supporting Information

XRD patterns, FE-SEM images, Charge–discharge curves, Cycling performances, Rate-capabilities.

AUTHOR INFORMATION

Corresponding Author: Hiroki Sakaguchi

*Email: sakaguch@chem.tottori-u.ac.jp

REFERENCES

(1) Myung, S.-T.; Maglia, F.; Park, K.-J.; Yoon, C. S.; Lamp, P.; Kim, S.-J.; Sun, Y.-K. Nickel-Rich Layered Cathode Materials for Automotive Lithium-Ion Batteries: Achievements and Perspectives. *ACS Energy Lett.* **2017**, 2, 196−223.

(2) Zhao, J.; Zaho, L.; Dimon, N.; Okada, S.; Nishida, T. Electrochemical and Thermal Properties of α-$NaFeO_2$ Cathode for Na-Ion Batteries. *J. Electrochem. Soc.* **2013**, *160*, A3077−A3081.

(3) Yabuuchi, N.; Iwatate, J.; Nishikawa, H.; Hitomi, S.; Okuyama, R.; Usui, R.; Yamada, Y.; Komaba, S. P2-type $Na_x[Fe_{1/2}Mn_{1/2}]O_2$ Made from Earth-Abundant Elements for Rechargeable Na Batteries. *Nat. Mater.* **2012**, *11*, 512−517.

(4) Barpanda, P.; Oyama, G.; Nishimura, S.; Chung, S.-C.; Yamada, A. A 3.8-V Earth-Abundant Sodium Battery Electrode. *Nat. Commun.* **2014**, *5*, 4358-1−8.

(5) Komaba, S.; Murata, W.; Ishikawa, T.; Yabuuchi, N.; Ozeki, T.; Nakayama, T.; Ogata, A.; Gotoh, K.; Fujiwara, K. Electrochemical Na Insertion and Solid Electrolyte Interphase for Hard-Carbon Electrodes and Application to Na-Ion Batteries. *Adv. Funct. Mater.* **2011**, *21*, 3859−3867.

(6) Dahbi, M.; Nakano, T.; Yabuuchi, N.; Ishikawa, T.; Kubota, K.; Fukunishi, M.; Shibahara, S.; Son, J.-Y.; Cui, Y.-T.; Komaba, S. *et al.* Sodium carboxymethyl cellulose as a potential binder for hard-carbon negative electrodes in sodium-ion batteries. *Electrochem. Commun.* **2014**, *44*, 66−69.

(7) Hasegawa, G.; Kanamori, K.; Kannari, N.; Ozaki, J.; Nakanishi, K.; Abe, T. Electrochemical Na Insertion and Solid Electrolyte Interphase for Hard-Carbon Electrodes and Application to Na-Ion Batteries. *ChemElectroChem* **2015**, *2*, 1917−1920.

(8) Qian, J.; Wu, X.; Cao, Y.; Ai, X.; Yang, H. High Capacity and Rate Capability of Amorphous Phosphorus for Sodium Ion Batteries. *Angew. Chem.* **2013**, *125*, 4731−4734.

(9) Wang, J. W.; Liu, X. H.; Mao, S. X.; Huang, J. Y.; Microstructural Evolution of Tin Nanoparticles during In Situ Sodium Insertion and Extraction. *Nano Lett.* **2012**, *12*, 5897−5902.

(10) Komaba, S.; Matsuura, Y.; Ishikawa, T.; Yabuuchi, N.; Murata, W.; Kuze, S. Redox Reaction of Sn-Polyacrylate Electrodes in Aprotic Na Cell. *Electrochem. Commun.* **2012**, *21*, 65−68.

(11) Yamamoto, T.; Nohira, T.; Hagiwara, R.; Fukunaga, A.; Sakai, S.; Nitta, K.; Inazawa, S. Charge–Discharge Behavior of Tin Negative Electrode for a Sodium Secondary Battery Using Intermediate Temperature Ionic Liquid Sodium Bis(fluorosulfonyl)amide–Potassium Bis(fluorosulfonyl)amide. *J. Power Sources* **2012**, *217*, 479−484.

(12) Shimizu, M.; Usui, H.; Fujiwara, K.; Yamane, K.; Sakaguchi, H. Electrochemical Behavior of SiO as An Anode Material for Na-Ion Battery. *J. Alloys Compd.* **2015**, *640*, 440−443.

(13) Lim, C.-H.; Huang, T.-Y.; Shao, P.-S.; Chien, J.-H.; Weng, Y.-T.; Huang, H.-F.; Hwang, B. J.; Wu, N.-L. Experimental Study on Sodiation of Amorphous Silicon for Use as Sodium-Ion Battery Anode. *Electrochim. Acta* **2016**, *211*, 265−272.

(14) Darwiche, A.; Marino, C.; Sougrati, M. T.; Fraisse, B.; Stievano, L.; Monconduit, L. Better Cycling Performances of Bulk Sb in Na-Ion Batteries Compared to Li-Ion Systems: An Unexpected Electrochemical Mechanism. *J. Am. Chem. Soc.* **2012**, *134*, 20805−20811.

(15) Wu, L.; Hu, X.; Qian, J.; Pei, F.; Wu, F.; Mao, R.; Ai, X.; Yang, H.; Cao, Y. Sb−C Nanofibers with Long Cycle Life as an Anode Material for High-Performance Sodium-Ion Batteries. *Energy Environ. Sci.* **2014**, *7*, 323−328.

(16) Lu, X.; Adkins, E. R.; He, Y.; Zhong, L.; Luo, L.; Mao, S. X.; Wang, C.-M.; Korgel, B. A. Germanium as a Sodium Ion Battery Material: In Situ TEM Reveals Fast Sodiation Kinetics with High Capacity. *Chem. Mater.* **2016**, *28*, 1236−1242.

(17) Jung, S. C.; Kim, H.-J.; Kang, Y.-J.; Han, Y.-K. A. Advantages of Ge anode for Na-ion batteries: Ge vs. Si and Sn. *J. Alloys Compd.* **2016**, *688*, 158−163.

(18) Shimizu, M.; Usui, H.; Sakaguchi, H. Electrochemical Na-Insertion/Extraction Properties of SnO Thick-Film Electrodes Prepared by Gas-Deposition. *J. Power Sources* **2014**, *248*, 378−382.

(19) Shimizu, M.; Usui, H.; Yamane, K.; Sakata, T.; Nokami, T.; Itoh, T.; Sakaguchi, H. Electrochemical Na-Insertion/Extraction Properties of Phosphorus Electrodes in Ionic Liquid Electrolytes. *Int. J. Electrochem. Sci.* **2015**, *10*, 10132−10144.

(20) Qian, J.; Xiong, Y.; Cao, Y.; Ai, X.; Yang, H. Synergistic Na-Storage Reactions in Sn_4P_3 as a High-Capacity, Cycle-stable Anode of Na-Ion Batteries. *Nano Lett.* **2014**, *14*, 1865−1869.

(21) Kim, Y.; Kim, Y.; Choi, A.; Woo, S.; Mok, D.; Choi, N.-S.; Jung, Y. S.; Ryu, J. H.; Oh, S. M.; Lee, K. T. Tin Phosphide as a Promising Anode Material for Na-Ion Batteries. *Adv. Mater.* **2014**, *26*, 4139−4144.

(22) Usui, H.; Sakata, T.; Shimizu, M.; Sakaguchi, H. Electrochemical Na-Insertion/Extraction Properties of Sn−P Anodes. *Electrochemistry* **2015**, *83*, 810−812.

(23) Shin, H.-S.; Jung, K.-N.; Jo, Y. N.; Park, M.-S.; Kim, H.; Lee, J.-W. Tin Phosphide-Based Anodes for Sodium-Ion Batteries: Synthesis via Solvothermal Transformation of Sn Metal and Phase-Dependent Na Storage Performance. *Sci. Reports* **2016**, *6*, 26195-1−26195-10.

(24) Zheng, L.; Dunlap, R. A.; Obrovac, M. N. The Electrochemical Reaction Mechanism of Tin Phosphide with Sodium. *J. Electrochem. Soc.* **2016**, *163*, A1188−A1191.

(25) Du, Z.; Dunlap, R. A.; Obrovac, M. N. Investigation of The Reversible Sodiation of Sn Foil by Ex-Situ X-ray Diffractometry and Mössbauer Effect Spectroscopy. *J. Alloys Compd.* **2014**, *617*, 271−276.

(26) Dahbi, M.; Yabuuchi, N.; Fukunishi, M.; Kubota, K.; Chihara, K.; Tokiwa, K.; Yu, X. F.; Ushiyama, H.; Yamashita, K.; Komaba, S. *et al.* Black Phosphorus as a High-Capacity, High-Capability Negative Electrode for Sodium-Ion Batteries: Investigation of the Electrode/Electrolyte Interface. *Chem. Mater.* **2016**, *28*, 1625−1635.

(27) Momma, K.; Izumi, F. VESTA 3 for Three-Dimensional Visualization of Crystal, Volumetric and Morphology Data. *J. Appl. Crystallogr.* **2011**, *44*, 1272−1276.

(28) Buzzeo, M. C.; Evans, R. G.; Compton, R. G. Non-Haloaluminate Room-Temperature Ionic Liquids in Electrochemistry - A Review. *ChemPhysChem* **2004**, *5*, 1106−1120.

(29) Shimizu, M.; Usui, H.; Suzumura, T.; Sakaguchi, H. Analysis of the Deterioration Mechanism of Si Electrode as a Li-Ion Battery Anode Using Raman Microspectroscopy. *J. Phys. Chem. C* **2015**, *119*, 2975−2982.

(30) Usui, H.; Shimizu, M.; Sakaguchi, H. Applicability of Ionic Liquid Electrolytes to $LaSi_2$/Si Composite Thick-Film Anodes in Li-Ion Battery. *J. Power Sources* **2013**, *235*, 29−35.

(31) Usui, H.; Masuda, T.; Sakaguchi, H. Li-Insertion/Extraction Properties of Si Thick-Film Anodes in Ionic Liquid Electrolytes Based on Bis(fluorosulfonyl)amide and Bis(trifluoromethanesulfonyl)amide Anions. *Chem. Lett.* **2012**, *41*, 521−522.